HHS Public Access

Author manuscript

Neuroimage. Author manuscript; available in PMC 2019 February 01.

Published in final edited form as:

Neuroimage. 2018 August 01; 176: 313–320. doi:10.1016/j.neuroimage.2018.05.015.

First demonstration of in vivo mapping for regional brain monoacylglycerol lipase using PET with [^{11}C]SAR127303

Tomoteru Yamasaki[a,*], **Wakana Mori**[a], **Yiding Zhang**[a], **Akiko Hatori**[a], **Masayuki Fujinaga**[a], **Hidekatsu Wakizaka**[a], **Yusuke Kurihara**[a,b], **Lu Wang**[c,d], **Nobuki Nengaki**[a,b], **Tomoyuki Ohya**[a], **Steven H. Liang**[d], and **Ming-Rong Zhang**[a]

[a]National Institute of Radiological Sciences, National Institutes for Quantum and Radiological Science and Technology, 4-9-1 Anagawa, Inage-ku, Chiba 263-8555, Japan

[b]SHI Accelerator Service Co. Ltd, 1-17-6 Osaki, Shinagawa-ku, Tokyo 141-0032, Japan

[c]Department of Nuclear Medicine and PET/CT-MRI Center, The First Affiliated Hospital of Jinan University, Guangzhou, Guangdong Province, 510630, China

[d]Division of Nuclear Medicine and Molecular Imaging, Department of Radiology, Massachusetts General Hospital & Harvard Medical School, Boston, MA, 02114, USA

Abstract

Monoacylglycerol lipase (MAGL) is a main regulator of the endocannabinoid system within the central nervous system (CNS). Recently, [^{11}C]SAR127303 was developed as a promising radioligand for MAGL imaging. In this study, we aimed to quantify regional MAGL concentrations in the rat brain using positron emission tomography (PET) with [^{11}C]SAR127303. An irreversible two-tissue compartment model (2-TCMi, $k_4 = 0$) analysis was conducted to estimate quantitative parameters (k_3, $K_i^{2\text{-}TCMi}$, and λk_3). These parameters were successfully obtained with high identifiability (< 10 %COV) for the following regions ranked in order from highest to lowest: cingulate cortex > striatum > hippocampus > thalamus > cerebellum > hypothalamus ≈ pons. In vitro autoradiographs using [^{11}C]SAR127303 showed a heterogeneous distribution of radioactivity, as seen in the PET images. The $K_i^{2\text{-}TCMi}$ and λk_3 values correlated relatively highly with in vitro binding ($r > 0.4$, $P < 0.005$). The $K_i^{2\text{-}TCMi}$ values showed high correlation and low underestimation (< 10%) compared with the slope of a Patlak plot analysis with linear regression (K_i^{Patlak}). In conclusion, we successfully estimated regional net uptake value of [^{11}C]SAR127303 reflecting MAGL concentrations in rat brain regions for the first time.

[*]Corresponding author: Tomoteru Yamasaki, PhD., Department of Radiopharmaceuticals Development, National Institute of Radiological Sciences, National Institutes for Quantum and Radiological Science and Technology, 4-9-1 Anagawa, Inage-ku, Chiba 263-8555, Japan. Tel: +81 43 206 4041; Fax: +81 43 206 3261; yamasaki.tomoteru@qst.go.jp.

Declaration of conflicting interests

The author(s) declare no potential conflicts of interest with respect to the research, authorship, and/or publication of this article.

Supplementary material

Supplementary material for this paper can be found at https://doi.org/10.1016/j.neuroimage.2018.05.015.

Keywords

monoacylglycerol lipase; net influx constant K_i; Patlak plot; positron emission tomography; two-tissue compartment model

Introduction

The endocannabinoid (eCB) system is a well-known neurotransmission network within the central and peripheral nervous system. Its functions are mainly regulated by two-types of G protein-coupled cannabinoid receptors, CB1 and CB2 (Woodhams et al., 2017). These receptors are stimulated by binding to endocannabinoids, such as 2-arachidoneylglycerol (2-AG) and anandamide (AEA). These endocannabinoids are produced on demand through stimulus-dependent cleavage of phospholipid precursors; they can modulate multiple physiological processes including pain, inflammation, appetite, memory, and emotion, and are terminated by enzymatic hydrolysis (Di Marzo, 2009). Among the endocannabinoids, 2-AG is generated by activation of phospholipase C and diacylglycerol lipase, which are linked with activation of Gq protein-coupled receptors such as group I metabotropic glutamate receptors, and are inactivated by monoacylglycerol lipase (MAGL) (Labar et al., 2010). Moreover, the concentration of 2-AG in the brain is very substantially higher than that of AEA. Recent emerging evidence indicates that 2-AG is an important signaling mediator, maintaining brain homeostasis by exerting its anti-inflammatory and neuroprotective effects in response to harmful insults via CB1/2 receptor-dependent and/or receptor-independent mechanisms (Xu and Chen, 2015). Against this background, the monitoring of MAGL as a modulator of 2-AG appears to be an important subject of study with regard to resolving disturbances in brain homeostasis.

Positron emission tomography (PET) is a well-known advanced molecular imaging technique that uses pharmaceuticals labelled with positron-emitting nuclides (e.g., ^{11}C, ^{18}F, and ^{15}O); it enables in vivo molecular information to be obtained via qualitative visualization and quantitative measurement of nuclide uptake. In vivo monitoring of MAGL with PET would enable investigations of the involvement of the eCB system in central nervous system (CNS) disorders. The first radioligands developed for MAGL imaging were reported in 2014 (Hicks et al., 2014). However, there were no useful PET ligands for MAGL imaging available at that time. Recently, several radioligands for MAGL have been developed (Wang et al., 2016a,b; Ahamed et al., 2017; Chen et al., 2018). Of these, [^{11}C]SAR127303 (Log$D$ = 3.69) showed high heterogeneous brain uptakes of radioactivity in PET studies using rats, which were significantly reduced by pretreatment with KML29, a potent inhibitor of MAGL (Wang et al., 2016b). These results strongly suggest that [^{11}C]SAR127303 displays specific and selective binding to MAGL. Moreover, a high brain uptake of [^{11}C]SAR127303 was also observed in a PET assessment using a nonhuman primate. The characteristics of the kinetics of [^{11}C]SAR127303 in rodent and nonhuman primate brains indicate irreversible binding to MAGL (Figure 1a) (Wang et al., 2016b). In this study, we aimed to estimate regional MAGL concentrations using quantitative PET analysis with [^{11}C]SAR127303 and subsequently making comparisons with in vitro binding of [^{11}C]SAR127303 on autoradiographs.

Materials and methods

General

All experiments were approved by the committee of the National Institutes for Quantum and Radiological Science and Technology (QST).

[^{11}C]SAR127303 was synthesized from a piperidine precursor with [^{11}C]$COCl_2$ in the presence of 1,2,2,6,6-pentamethylpiperidine, followed by treatment with 1,1,1,3,3,3-hexafluoro-2-propanol, as described previously (Wang et al., 2016a,b). At the end of synthesis, 0.47 ± 0.33 GBq (n = 7) of [^{11}C]SAR12703 was obtained with > 99% radiochemical purity and 89.4 ± 58.9 GBq/μmol molar activity; this was suitable for the animal experiments.

Animals

Male Sprague Dawley (SD) rats (Japan SLC, Shizuoka, Japan) were kept in a temperature-controlled environment with a 12-h light/dark cycle and were fed on a standard diet (MB-1/Funabashi Farm, Chiba, Japan). Animal experiments were performed according to the recommendations of the Committee for the Care and Use of Laboratory Animals in QST and the ARRIVE guidelines (http://www.nc3rs.org/ARRIVE).

PET procedure

To develop an optimal quantitative method, brain PET examinations with [^{11}C]SAR127303 were performed on SD rats (n = 7, male, 8–10 weeks old, 330 ± 45 g). Prior to PET scanning, each rat had a polyethylene catheter (FR2/Imamura, Tokyo, Japan) inserted into the left femoral artery for blood sampling and a 24-gauge catheter (Terumo Medical Products, Tokyo, Japan) inserted into the tail vein for a bolus injection, with the catheter insertions being performed under anesthesia (1.5%–2% isoflurane in air). Subsequently, rats were placed in a small-animal PET scanner (Inveon/Siemens, Knoxville TN, USA) and injected with a bolus of [^{11}C]SAR127303 (37–50 MBq, 0.5–1.0 pmol in 1.0 mL saline) at a rate of 0.5 mL/min using a syringe pump (PHD 2000/Harvard Apparatus, MA, USA) via the tail vein catheter. Dynamic emission scans were acquired in a three-dimensional list mode for 60 min (10 s × 12 frames, 20 s × 3 frames, 30 s × 3 frames, 1 min × 3 frames, 2.5 min × 3 frames, and 5 min × 8 frames). PET dynamic images were reconstructed with filtered back projection using a Hanning filter with a Nyquist cut-off of 0.5 cycle/pixel.

Arterial blood samples (50–400 μL, total 1.8 mL) were collected at 20, 40, 60, 80, 100, 110, 120, 130, 140, 160 s, and 3, 4, 5, 10, 15, 30, 45, and 60 min after the injection. The radioactivity in the whole blood and plasma was counted using a 1480 Wizard autogamma scintillation counter (Perkin-Elmer, Waltham, MA, USA). Radioactivity was corrected for decay.

Metabolite analysis

Plasma samples (50–200 μL) separated at selected time points (1, 5, 15, 30, 45, and 60 min) were spiked with 20% (v/v) of a 50% aqueous acetic acid solution. The mixture was collected in a test tube containing an equivalent volume of acetonitrile (MeCN) and then

vortexed for 15 s followed by centrifugation at 20 000 *g* for 2 min for deproteinization. An aliquot of the supernatant was injected into a radio-high-performance liquid chromatography (HPLC) system (Shimadzu, Kyoto, Japan) equipped with a radioactivity detector (Takei et al., 2001), and analyzed using a Capcell Pack C18 column (4.6 mm i.d. × 250 mm; Shiseido, Tokyo, Japan) with MeCN/H_2O/trifluoroacetic acid (7/3/0.01, v/v/v) at 1.5 mL/min. The percentage of [^{11}C]SAR127303 (retention time = 8.7 min) to total radioactivity (corrected for decay) on the HPLC chromatogram was calculated as % = (peak area of [^{11}C]SAR127303/total peak area) × 100. To estimate deposit of unmetabolized [^{11}C]SAR127303 in plasma protein pellet, [^{11}C]SAR127303 (1 MBq, 10 μL) was incubated with plasma sample (100 μL) for 5 min at room temperature, vortexed, and deproteinnized as described above. After centrifuge, the radioactivities in the supernatant and plasma pellets were counted using a 1480 Wizard autogamma scintillation counter. A metabolite-corrected plasma curve was generated from the product of the plasma activity and the unchanged form of the [^{11}C]SAR127303 fraction.

Data analysis

Summed PET images acquired between 0 and 60 min after the injection of [^{11}C]SAR127303 were produced using PMOD software (version 3.4, PMOD Technologies, Zurich, Switzerland). Volumes of interest (VOIs) were manually drawn on the cingulate cortex, striatum (caudate/putamen), hippocampus, thalamus, hypothalamus, pons, and cerebellum, by reference to MRI templates of SD rat brain (Yamasaki et al., 2016). The respective tissue time-activity curves (tTACs) for each VOI were then derived from the dynamic PET images. The radioactivity was decay corrected to the injection time and expressed as a standardized uptake value (SUV), which was normalized to the injected radioactivity and body weight.

$$SUV = (radioactivity\ of\ tissue / injected\ radioactivity) \times body\ weight(g) \quad (1)$$

Kinetic analysis

Kinetic analyses with arterial blood sampling were performed using a one-tissue compartment model (1-TCM), an irreversible two-tissue compartment model (2-TCMi) (Figure 1B) (Rusijan et al., 2013) and Patlak graphical analysis (Patlak plot) (Patlak et al., 1983) using the metabolite-corrected plasma curve as an input function. In the 2-TCMi model, three rate constants (K_1–k_3) were estimated by nonlinear-least-squares (NLS) fitting and the K_i and λk_3 values (Rusijan et al., 2013) for each region were calculated:

$$K_i = \frac{K_1 k_3}{k_2 + k_3} \quad (2)$$

$$\lambda k_3 = \frac{K_1}{k_2} \times k_3 \quad (3)$$

The blood volume fraction (vB) in the rat brain was fixed at 2% and time delay (5.0 ± 2.1 s) in tTAC was automatically estimated from time delay of TAC in the whole brain from the time course of the input function using PMOD software. In the Patlak plot, the K_i value of each region was estimated as the slope of a regression line of points between 15 and 60 min:

$$\frac{C_T(t)}{C_P(t)} = K_i \frac{\int_0^t C_P(\tau)d\tau}{C_p(t)} + V \quad (4)$$

where C_T and C_P express radioactive concentrations in tissue and plasma respectively. The slope and intercept must be interpreted according to the underlying compartment model. For the irreversible radioligand mentioned, the slope equals K_i and represents the influx, while the intercept V is combination of vB and the reversible compartment (C_1) distribution volume.

In vitro autoradiography

Sagittal brain sections (20 μm) were prepared from three rats (male, 8 weeks old) different from PET assessments. Briefly, rats were killed by cervical dislocation under anesthesia (3% isoflurane in air) and their brains were quickly removed, frozen in crushed dry ice, and sliced into sections using a cryostat (HM560; Carl Zeiss, Oberkochen, Germany). The sections from all rats were preincubated for 10 min in 20 mM Tris-HCl buffer (pH 8.0) containing 1 mM EDTA and 0.01% Triton X-100 at room temperature. After preincubation, the sections were incubated for 30 min at room temperature in fresh buffer containing [^{11}C]SAR127303 (7.6 MBq, 0.1 nM). After incubation, brain sections were washed (3 × 2 min) with cold buffer, immersed in cold distilled water, and then dried with cold air. The sections were then placed in contact with imaging plates (BAS-MS2025, FUJIFILM, Tokyo, Japan) for 60 min. Autoradiograms were obtained and the photo-stimulated luminescence (PSL) values of the ROIs were measured using a Bio-Imaging Analyzer System (BAS5000, FUJIFILM).

Statistical methods

Goodness of fit was evaluated using the Akaike Information Criterion (AIC) (Akaike., 1974) and the Model Selection Criterion (MSC) (Handbook MS, 1995).Values are given as mean ± standard deviation. The percentage of coefficients of variation (%COV) was estimated from the diagonal of the covariance matrix of the fitting. All data analyses were performed using GraphPad Prism v5.0 (GraphPad Software, La Jolla, CA, USA).

Results

Plasma input function

The deposit of unmetabolized [^{11}C]SAR127303 in plasma protein pellet was 3.6 ± 0.6% (n = 3) through the metabolite analysis. Therefore, it was considered that there was no risk underestimating the % metabolism.

Figure 2 shows time-curves of radioactivity for the whole blood, plasma, and metabolite-corrected plasma input function. [^{11}C]SAR127303 was quickly metabolized to two polar metabolites (Supplementary Figure S1). The time course for the unchanged form of [^{11}C]SAR127303 was 89.2% ± 9.4%, 30.9% ± 3.9%, 14.0% ± 6.1%, 7.2% ± 5.6%, 3.3% ± 1.5%, and 1.4% ± 0.6% at 1, 5, 15, 30, 45, and 60 min post injection respectively. The averaged metabolite-corrected input curve of [^{11}C]SAR127303 exhibited an SUV of 1.8 ± 0.4, peaking at 2 min post injection and quickly decreasing afterwards. At 30 min after the injection, the input curve had an SUV of less than 0.1 and then gradually decreased until the scan finished. At the end of the PET scan, the unchanged [^{11}C]SAR127303 remaining in the plasma had an SUV of 0.02 ± 0.02.

Distribution of radioactivity across brain regions

After the [^{11}C]SAR127303 injection, all of the rats showed uptake of radioactivity in the brain. High uptake was observed in the cingulate cortex, striatum, hippocampus, cerebellum, and thalamus, whereas radioactive uptake in the hypothalamus and pons/medulla was low (these regions are ranked in order of high to low uptake of radioactivity according to the TACs; Supplementary Figure S2). As expected from the known distribution of MAGL in rat brain (Dinh et al., 2002), the distribution of radioactivity was widespread and fairly uniform within the cingulate cortex, hippocampus, and cerebellum.

In the cingulate cortex with the highest radioactive uptake, the radioactivity rapidly penetrated into the brain, subsequently showed a gentle decline until 5–15 min, and was then retained until the end of the scan. On the other hand, radioactivity in the pons with the lowest radioactive uptake showed a slow decrease until 30 min after rapid penetration into the brain, which was a constant until the end of the scan (Figure 3). Additionally, these kinetics strongly supported that two polar metabolites of [^{11}C]SAR127303 in the plasma (Supplementary Figure S1) could not enter the brain.

Kinetic analysis

Figure 3 shows representative NLS fitting curves based on 1-TCM (K_1 = 0.53 mL/cm^3/min, k_2 = 0.02 /min for the cingulate cortex), 2-TCMi (K_1 = 0.83 mL/cm^3/min, k_2 = 0.20 /min, and 0.10 /min for the cingulate cortex) (a), and a Patlak plot with linear regression (b). The 1-TCM was obviously insufficient to fit the TACs (Figure 3a). Moreover, respective the averaged AIC and MSC scores for goodness of fit for 1-TCM vs. 2-TCMi were 95.3 vs. −18.4 and 1.6 vs. 5.1 for the cingulate cortex and 121.3 vs. −47.1 and 0.8 vs. 5.9 for the pons. These results supported that 2-TCMi fits in PET with [^{11}C]SAR127303 were better than 1-TCM.

Table 1 shows the results of the full kinetic parameters estimated by 2-TCMi. The three direct parameters (K_1, k_2, and k_3) could be clearly estimated in all brain regions, with a 1.2–1.8 %COV for K_1, a 3.5–7.4 %COV for k_2, and a 3.4–6.7 %COV for k_3. As the three parameters (K_1–k_3) were highly distinguishable, the composite parameters (K_1/k_2, $K_1^{2\text{-}TCMi}$, and λk_3) were also well defined, with K_1/k_2 having a 2.5–5.9 %COV, $K_1^{2\text{-}TCMi}$ a 4.5–8.7 %COV, and λk_3 a 4.2–9.0 %COV. The ranked order of the brain regions according to the parameters (k_3, $K_1^{2\text{-}TCMi}$, and λk_3) reflecting MAGL concentrations was: cingulate cortex >

striatum > hippocampus > thalamus > cerebellum > hypothalamus > pons. These results showed high correlation ($r > 0.999$) with the K_1^{Patlak} values, which were obtained with high identifiability by linear regression (0.6–1.3 %COV).

In vitro autoradiography

To investigate in vitro binding of [^{11}C]SAR127303 to MAGL, we performed in vitro autoradiography using sagittal brain sections from three rats. Figure 4 shows the representative autoradiogram (Figure 4a) of [^{11}C]SAR127303 and the concentration of radioactivity (PSL/mm^2) in the different brain regions (Figure 4b). The distribution pattern of radioactivity was heterogeneous, with the highest radioactivity concentration occurring in the cingulate cortex. Moderate concentrations of radioactivity were seen in the hippocampus and cerebellum, but only weak signals were detected in the striatum and thalamus. Slight binding of [^{11}C]SAR127303 was observed in the hypothalamus and pons. These distribution patterns of [^{11}C]SAR127303 closely corresponded with the biological localization of MAGL (Dinh et al., 2002).

Correlation between kinetic parameters and in vitro binding of [^{11}C]SAR127303

Figure 5 shows scatter plots of the kinetic parameters (k_3, $K_1^{2\text{-}TCMi}$, λk_3, and K_1^{Patlak}) and the in vitro binding of the autoradiograms using [^{11}C]SAR127303. Of the parameters based on 2-TCMi, $K_1^{2\text{-}TCMi}$ and λk_3 indicated relatively high correlations with in vitro binding of [^{11}C]SAR127303, with correlation coefficients (r) of 0.521 ($P < 0.001$) and 0.474 ($P < 0.001$) respectively. Conversely, the direct parameter k_3 reflecting MAGL concentration exhibited a poor correlation with in vitro binding of [^{11}C]SAR127303, with an r of 0.176 ($P = 0.226$). However, the K_1^{Patlak} values acquired from the linear regression indicated the highest correlation ($r = 0.549$, $P < 0.001$) with in vitro binding.

Parametric PET images based on net uptake value

Figure 6 shows representative parametric PET/MRI images based on K_1^{Patlak}. In the K_1-based images, the strongest signal was observed in the cingulate cortex. Relatively strong signals were also detected in the striatum, hippocampus, thalamus, and cerebellum, while low signals were found in the hypothalamus and pons. This distribution pattern of K_1-based signals corresponded strongly with the distribution pattern of in vitro binding of [^{11}C]SAR127303, which suggests that K_1-based parametric images could reflect the availability of MAGL for [^{11}C]SAR127303.

Discussion

The current study presents the first quantitative visualization of net uptake value for regional MAGL in the rat brain using PET with [^{11}C]SAR127303.

SAR127303 is known as a ‘suicide’ enzyme inhibitor that covalently labels the enzyme MAGL; it was designed to produce irreversible acylation of serine hydrolase (Figure 1a) (Griebel et al., 2015). It was anticipated that the compartment model should include an irreversible trapping compartment (Figure 1b). Although the goodness-of-fit (AIC and MSC) of 2-TCM (the compartment model for a reversible ligand) was superior to that of 2-TCMi

(data not shown), the rate constant k_4 in 2-TCM was very small (< 0.01/min) with poor identifiability (> 25%COV). The best result of the goodness-of-fit was determined in 3-TCMi isolating free and nonspecific binding (data not shown). However, identifiability of individual rate constants in 3-TCMi was very low due to more complex kinetic model. Therefore, we consider that 2-TCMi would be a reasonable compartment model for quantitative PET analysis using [^{11}C]SAR127303.

In general, the blood flow or transport rate across the plasma membrane may limit the net amount of an irreversible radioligand of tracer uptake. When the irreversible trapping rate is too high ($k_3 >> k_2$), the limitation effect depends on the delivery of tracer to tissue (K_1), and therefore, sensitivity to changes in net uptake value may be poor. Previous reports have suggested that the range of the suitable ratios for k_3/k_2 is within a single order of magnitude, with the optimal ratio for determining k_3 typically to be between 0.1 and 1.0 (Ohya et al., 2011; Koeppe et al., 1999). Values of k_3 that were either greater than k_2 or less than 0.05 times k_2 have provided poor results (Koeppe et al., 1991, 1996). In our study, the ratios of k_3/k_2 in each brain region were 0.3–0.7, which were adequate for determination of k_3. The irreversible compartment model (2-TCMi) provides three parameters based on k_3 to measure changes in MAGL concentration (B_{max}). In this study, direct k_3, $K_i^{2\text{-}TCMi}$, and λk_3 were clearly identifiable (Table 1). Additionally, the ranked-order values of these parameters strongly corresponded with the order of radioactive accumulation on the in vitro autoradiographs, which in turn correlated with the previous immunoactive distribution of MAGL (Figure 4). However, the direct k_3 values were relatively low (< 0.1 /min) and showed high individual variations, despite the high identifiability. Thereby, the correlation between the direct k_3 values and in vitro binding of [^{11}C]SAR127303 was poor (Figure 5a). These results suggested that direct k_3 as absolute value would be unreasonable parameter due to too high sensitivity to individual variations of MAGL concentrations, which was also supported by high correlation ($r = 0.553$, $P < 0.001$) of the relative k_3 values (the ratio to k_3 of whole brain) with in vitro binding of [^{11}C]SAR127303 (see in Supplementary Figure S3). In contrast, K_i and λk_3 values including K_1 and k_2 could more stably estimate MAGL concentration in this study, because effects of individual variations in kinetic parameters would be kept to the minimum (Figures 5b and 5c).

On the basis of equation 4, the K_i values show a nonlinear response to the k_3/k_2 ratios. When the ratio of k_3/k_2 is over 10, the K_i value is close to the K_1 value. To the contrary, when the k_3/k_2 ratio is less than 0.1, the K_i value is close to zero (Supplementary Figure S4a). However, the λk_3 value depends linearly on the ratio of k_3/k_2, because it contains the ratio of K_1/k_2, and also the ratio of the correlated parameters k_2 and k_3 (Supplementary Figure S4a). Thus, the λk_3 value has been proposed as a parameter for quantification of irreversible radioligands (Dewey et al., 1991; Logan et al., 1991; Rusjan et al., 2013). However, in this study, the correlation of λk_3 values with in vitro binding of [^{11}C]SAR127303 was inferior to that of the $K_i^{2\text{-}TCMi}$ values (Figure 5). This may have been caused by high variation in the k_3/k_2 ratio, because the variation in λk_3 is larger than that of K_i (Supplementary Figure S4). Therefore, in the case of [^{11}C]SAR127303, the K_i value is a superior index to the λk_3 value for estimating MAGL concentration.

K_i values were also acquired by Patlak plot. In the present study, K_i^{Patlak} values correlated highly with $K_i^{2\text{-}TCMi}$ values, while presenting a small underestimation (< 10%). In general, violation of the assumptions of the Patlak plot could induce a large underestimation of the K_i value. In the case of [^{11}C]SAR127303, a plateau in the ratio of the non-displaceable compartment to the plasma was quickly achieved ($t^* \leq 10$ min; Figure 3b). Therefore, the K_i^{Patlak} values in this study were acquired using a simpler method with higher identifiability than the $K_i^{2\text{-}TCMi}$ value (Table 1). Moreover, the parametric PET images based on K_i^{Patlak} values allowed successful visualization of the regional net uptake value corresponding with the in vitro binding of [^{11}C]SAR127303 with MAGL (Figure 6). Thus, this in vivo quantitative technique for visualizing net uptake value for MAGL concentration using [^{11}C]SAR127303 PET should facilitate the further understanding of several disorders involving MAGL.

In general, the Patlak plot is widely used to estimate the available dose of PET tracer, such as [^{18}F]FDG, [^{11}C]methionine, and [^{18}F]FET, in the tumor. Moreover, several reports using these PET tracers showed high correlation between the K_i^{Patlak} value and SUV value (Lindholm et al., 1993; Bolcaen et al., 2016). Similarly, the K_i^{Patlak} value and SUV value in this study showed high correlation ($r > 0.9$) in an individual rat. However, the absolute value of SUV showed no relationship with K_i^{Patlak} value (Supplementary Figure S5a). These results suggested that SUV value not reflect net uptake value of [^{11}C]SAR127303, but displayed the order of regional concentrations of MAGL. The ratio of SUV (SUVR) showed relatively high correlation ($r = 0.567$) to K_i^{Patlak} value (Supplementary Figure S5b), which might indicate potential usefulness as noninvasive quantitative index for MAGL concentrations.

In conclusion, we demonstrated quantification of net uptake value for brain MAGL concentration using PET with [^{11}C]SAR127303. The kinetic parameters (k_3, K_i, and λk_3) were obtained from an irreversible compartment model with high identifiability, and corresponded with the in vitro distribution of MAGL in the rat brain. Of these parameters, the K_i value showed the highest association with the in vitro binding of [^{11}C]SAR127303. In addition, the K_i value based on a simple method (Patlak plot) exhibited a small underestimation but superior identifiability when compared with the K_i value based on 2-TCMi. By using the K_i^{Patlak} value, we succeeded in achieving the first demonstration of in vivo mapping for MAGL concentrations in the healthy rat brain using PET.

Supplementary Material

Refer to Web version on PubMed Central for supplementary material.

Acknowledgments

We thank the staff of the National Institute of Radiological Sciences for their support with cyclotron operation, radioisotope production, radiosynthesis, and animal experiments. We thank Karl Embleton, PhD, from Edanz Group (www.edanzediting.com/ac) for editing a draft of this manuscript.

Funding

This study was supported by the Grants-in-Aid for Scientific Research [Basic Research C: 17K10461] from the Ministry of Education, Culture, Sports, Science and Technology of the Japanese Government.

References

1. Akaike H. A new look at the statistical model identification. IEEE. Trans. Auto. Cont. 1974; 19:8.
2. Ahamad M, Attili B, van Veghel D, Ooms M, Berben P, Celen S, Koole M, Declercq L, Savinainen JR, Laitinen JT, Verbruggen A, Bormans G. Synthesis and preclinical evaluation of [11C]MA-PB-1 for in vivo imaging of brain monoacylglycerol lipase (MAGL). Eur. J. Med. Chem. 2017; 136:104–113. [PubMed: 28486208]
3. Bolcaen J, Lybaert K, Moerman L, Descamps B, Deblaere K, Boterberg T, Kalala JP, Van den Broecke C, De Vos F, Vanhove C, Goethals I. Kinetic modeling and graphical analysis of 18F-fluoromethylcholine (FCho), 18F-fluoroethyltyrosine (FET) and 18F-fluorodeoxyglucose (FDG) PET for the fiscrimination between high-grade glioma and radiation necrosis in rats., 2016. PLoS One. 11(8):e0161845. [PubMed: 27559736]
4. Cheng R, Mori W, Ma L, Alhouayek M, Hatori A, Zhang Y, Ogasawara D, Yuan G, Chen Z, Zhang X, Shi H, Yamasaki T, Xie L, Kumata K, Fujinaga M, Nagai Y, Minamimoto T, Svensson M, Wang L, Du Y, Ondrechen MJ, Vasdev N, Cravatt BF, Fowler C, Zhang MR, Liang SH. In vitro and in vivo evaluation of 11C-labeled azetidine-carboxylates for imaging monoacylglycerol lipase by PET imaging studies. J. Med. Chem. 2018; doi: 10.1021/acs.jmedchem.7b01400
5. Dewey SL, Logan J, Wolf AP, Brodie JD, Angrist B, Fowler JS, Volkow ND. Amphetamine induced decreases in (^{18}F)-N-methylspiroperidol binding in the baboon brain using positron emission tomography (PET). Synapse. 1991; 7:324–327. [PubMed: 2042113]
6. Di Marzo V. The endocannabinoid system: Its general strategy of action, tools for its pharmacological manipulation and potential therapeutic exploitation. Pharmacol. Res. 2009; 60:77–84. [PubMed: 19559360]
7. Dinh TP, Carpenter D, Leslie FM, Freund TF, Katona I, Sensi SL, Kathuria S, Piomelli D. Brain monoglyceride lipase participating in endocannabinoid inactivation. Proc. Natl. Acad. Sci. U S A. 2002; 99:10819–10824. [PubMed: 12136125]
8. Griebel G, Pichat P, Beeske S, Leroy T, Redon N, Jacquet A, Françon D, Bert L, Even L, Lopez-Grancha M, Tolstykh T, Sun F, Yu Q, Brittain S, Arlt H, He T, Zhang B, Wiederschain D, Bertrand T, Houtmann J, Rak A, Vallée F, Michot N, Augé F, Menet V, Bergis OE, George P, Avenet P, Mikol V, Didier M, Escoubet J. Selective blockade of the hydrolysis of the endocannabinoid 2-arachidonoylglycerol impairs learning and memory performance while producing antinociceptive activity in rodents. Sci. Rep. 2015; 5:7642. [PubMed: 25560837]
9. Handbook MS. rev., 1995. 7EEF. MicroMath, Inc; Salt Lake City: p. 467
10. Hicks JW, Parkes J, Tong JC, Houle S, Vasdev N, Wilson AA. Radiosynthesis and ex vivo evaluation of [C-11-carbonyl]carbamate- and urea-based monoacylglycerol lipase inhibitors. Nucl. Med. Biol. 2014; 41:688–694. [PubMed: 24969632]
11. Koeppe RA, Frey KA, Snyder SE, Meyer P, Kilbourn MR, Kuhl DE. Kinetic modeling of N-[^{11}C]methylpiperidin-4-yl propionate: alternatives for analysis of an irreversible positron emission tomography trace for measurement of acetylcholinesterase activity in human brain. J. Cereb. Blood. Flow. Metab. 1999; 19:1150–1163. [PubMed: 10532640]
12. Koeppe RA, Frey KA, Vander Borght TM, Karlamangla A, Jewett DM, Lee LC, Kilbourn MR, Kuhl DE. Kinetic evaluation of [^{11}C]dihydrotetrabenazine by dynamic PET: measurement of vesicular monoamine transporter. J. Cereb. Blood. Flow. Metab. 1996; 16:1288–1299. [PubMed: 8898703]
13. Koeppe RA, Holthoff VA, Frey KA, Kilbourn MR, Kuhl DE. Compartmental analysis of [^{11}C]flumazenil kinetics for the estimation of ligand transport rate and receptor distribution using positron emission tomography. J. Cereb. Blood. Flow. Metab. 1991; 11:735–744. [PubMed: 1651944]
14. Labar G, Wouters J, Lambert DM. A Review on the Monoacylglycerol Lipase: At the Interface Between Fat and Endocannabinoid Signalling. Curr. Med. Chem. 2010; 17:2588–2607. [PubMed: 20491633]
15. Lindholm P, Leskinen-Kallio S, Minn H, Bergman J, Haaparanta M, Lehikoinen P, Någren K, Ruotsalainen U, Teräs M, Joensuu H. Comparison of fluorine-18-fluorodeoxyglucose and carbon-11-methionine in head and neck cancer. J. Nucl. Med. 1993; 34:1711–1716. [PubMed: 8410288]

16. Logan J, Dewey SL, Wolf AP, Fowler JS, Brodie JD, Angrist B, Volkow ND, Gatley SJ. Effects of endogenous dopamine on measures of [^{18}F]N-methylspiroperidol binding in the basal ganglia: comparison of simulations and experimental results from PET studies in baboons. Synapse. 1991; 9:195–207. [PubMed: 1685599]

17. Ohya T, Okamura T, Nagai Y, Fukushi K, Irie T, Suhara T, Zhang MR, Fukumura T, Kikuchi T. Effect of radiolabeled metabolite elimination from the brain on the accuracy of cerebral enzyme activity estimation using positron emission tomography with substrate tracers. Neuroimage. 2011; 56:1105–1110. [PubMed: 21324368]

18. Patlak CS, Blasberg RG, Fenstermacher JD. Graphical evaluation of blood-to-brain transfer constants from multiple-time uptake data. J. Cereb. Blood. Flow. Metab. 1983; 3:1–7. [PubMed: 6822610]

19. Rusjan PM, Wilson AA, Mizrahi R, Boileau I, Chavez SE, Lobaugh NJ, Kish SJ, Houle S, Tong J. Mapping human brain fatty acid amide hydrolase activity with PET. J. Cereb. Blood. Flow. Metab. 2013; 33:407–414. [PubMed: 23211960]

20. Takei M, Kida T, Suzuki K. Sensitive measurement of positron emitters eluted from HPLC. Appl. Radiat. Isot. 2001; 55:229–234. [PubMed: 11393764]

21. Wang C, Placzek MS, Van de Bittner GC, Schroeder FA, Hooker JM. A novel radiotracer for imaging monoacylglycerol lipase in the brain using positron emission tomography. ACS. Chem. Neurosci. 2016a; 7:484–489. [PubMed: 26694017]

22. Wang L, Mori W, Cheng R, Yui JJ, Hatori A, Ma LL, Zhang Y, Rotstein BH, Fujinaga M, Shimoda Y, Yamasaki T, Xie L, Nagai Y, Minamimoto T, Higuchi M, Vasdev N, Zhang MR, Liang SH. Synthesis and preclinical evaluation of sulfonamido-based [C-11-carbonylcarbamates and ureas for imaging monoacylglycerol lipase. Theranostics. 2016b; 6:1145–1159. [PubMed: 27279908]

23. Woodhams SG, Chapman V, Finn DP, Hohmann AG, Neugebauer V. The cannabinoid system and pain. Neuropharmacology. 2017; 124:105–120. [PubMed: 28625720]

24. Xu JY, Chen C. Endocannabinoids in synaptic plasticity and neuroprotection. Neuroscientist. 2015; 21:152–168. [PubMed: 24571856]

25. Yamasaki T, Fujinaga M, Kawamura K, Furutsuka K, Nengaki N, Shimoda Y, Shiomi S, Takei M, Hashimoto H, Yui J, Wakizaka H, Hatori A, Xie L, Kumata K, Zhang MR. Dynamic changes in striatal mGluR1 but not mGluR5 during pathological progression of Parkinson's disease in human alpha-synuclein A53T transgenic rats: a multi-PET imaging study. J. Neurosci. 2016; 36:375–384. [PubMed: 26758830]

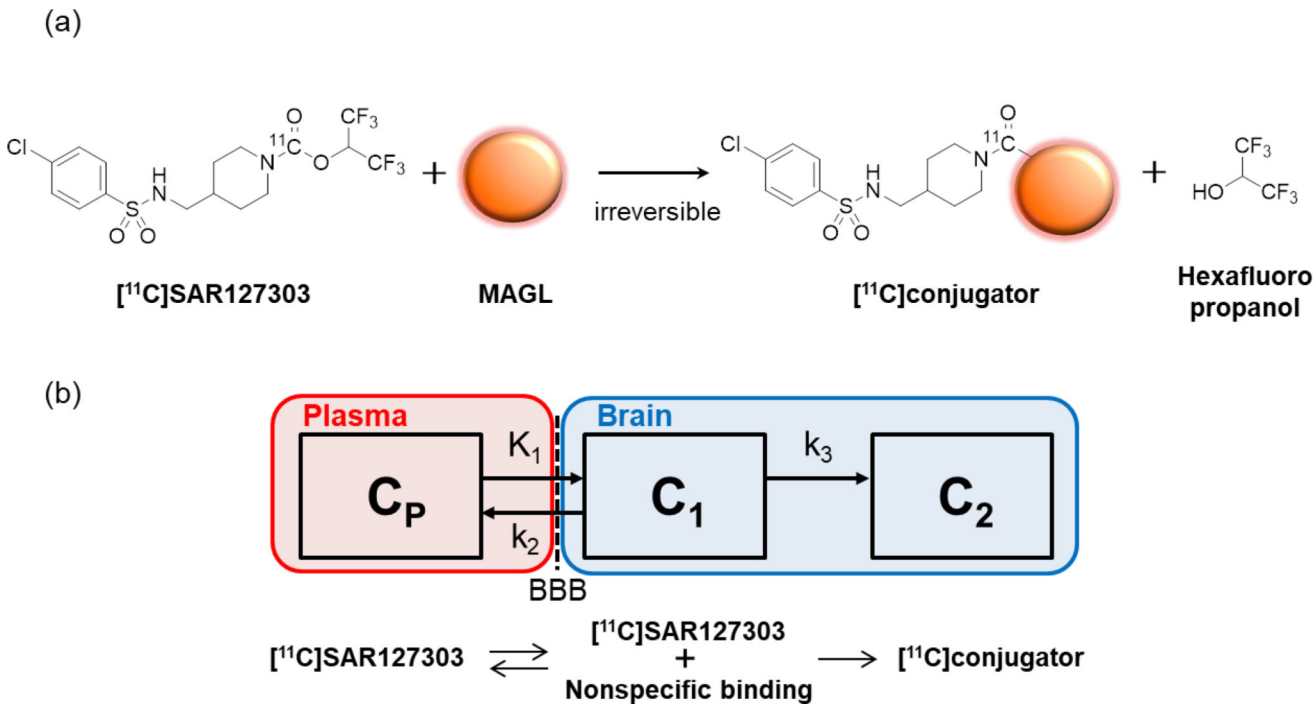

Figure 1.

Mechanism of action for binding of [^{11}C]SAR127303 to monoacylglycerol lipase (MAGL) (a), and the irreversible two-tissue compartment model used in this study (b).

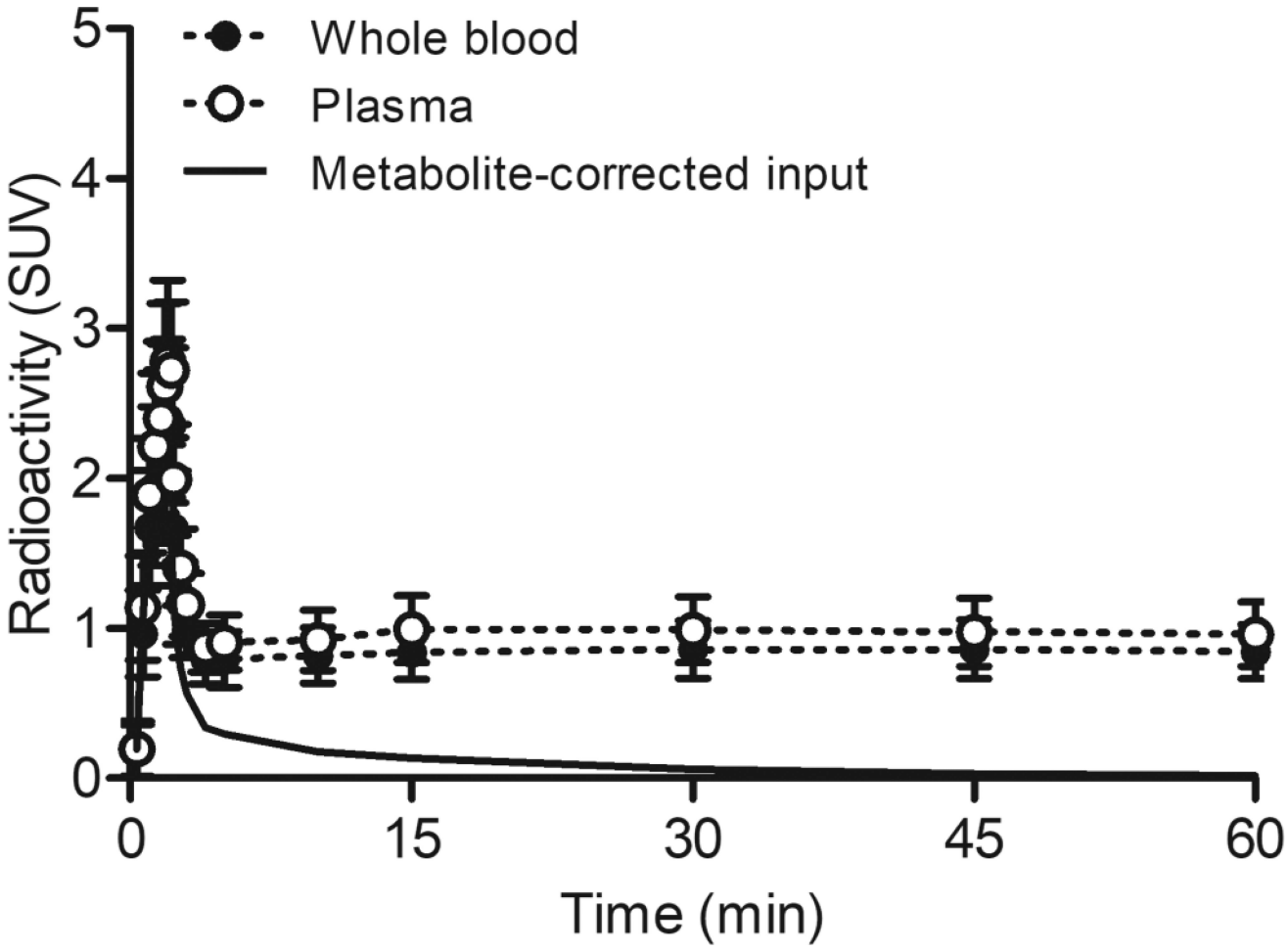

Figure 2.
Time-curves of radioactivity in the whole blood, plasma, and metabolite-corrected plasma input function. Radioactivity is expressed as SUV.

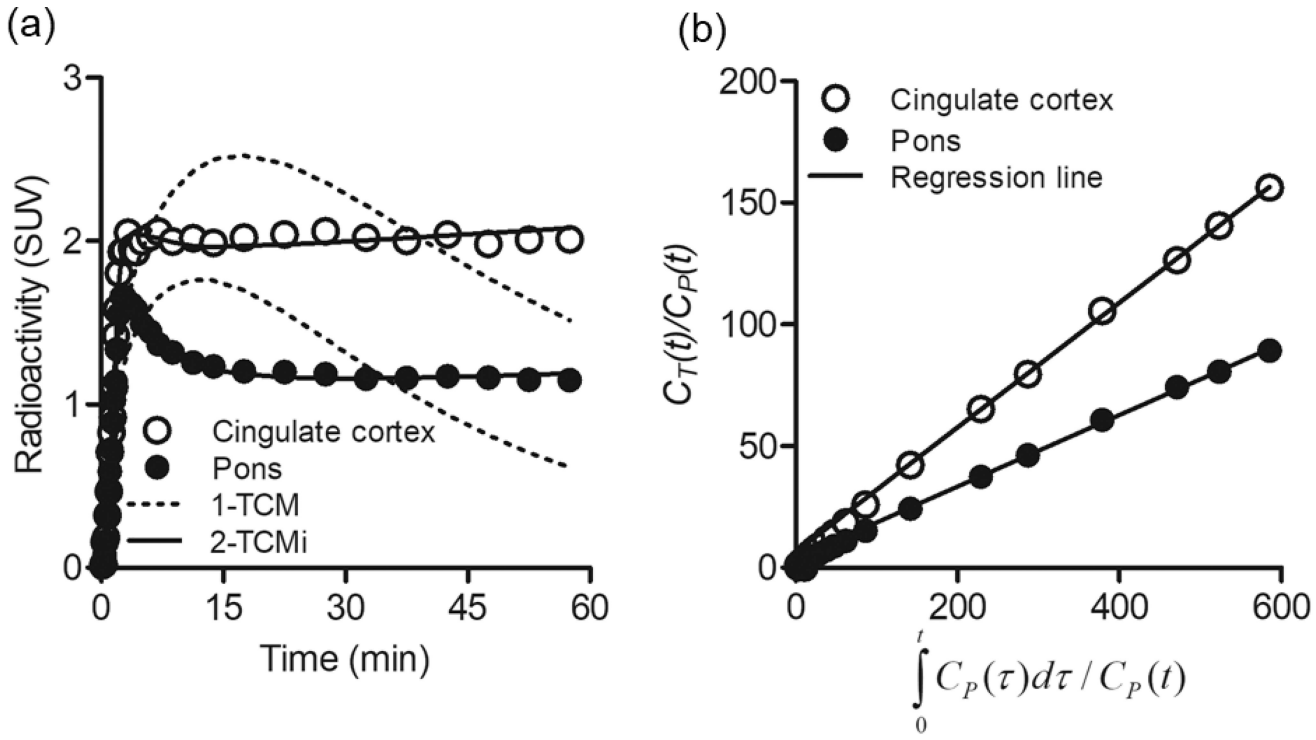

Figure 3.

Representative time-activity curves with compartment model fittings (a) and Patlak plot (b) in the cingulate cortex (open circles) and pons (solid circles). Radioactivity is expressed as SUV.

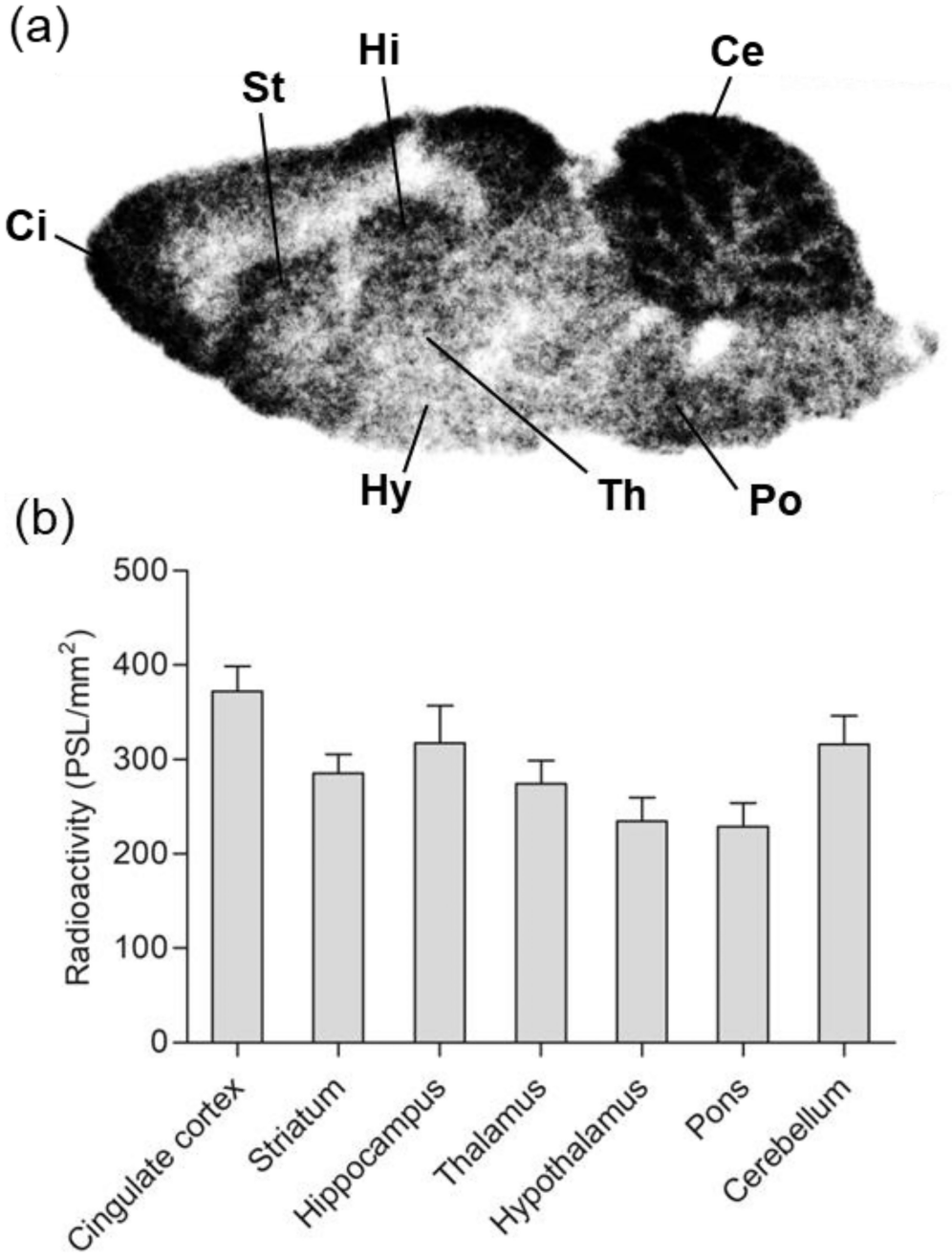

Figure 4.

Representative in vitro autoradiograph (a) and quantitative values in the different brain regions (b). Regions of interest were drawn as follows: Ci, cingulate cortex; St, striatum; Hi, hippocampus; Th, thalamus; Hy, hypothalamus; Ce, cerebellum; Po, pons. Radioactivity is expressed as PSL/mm^2.

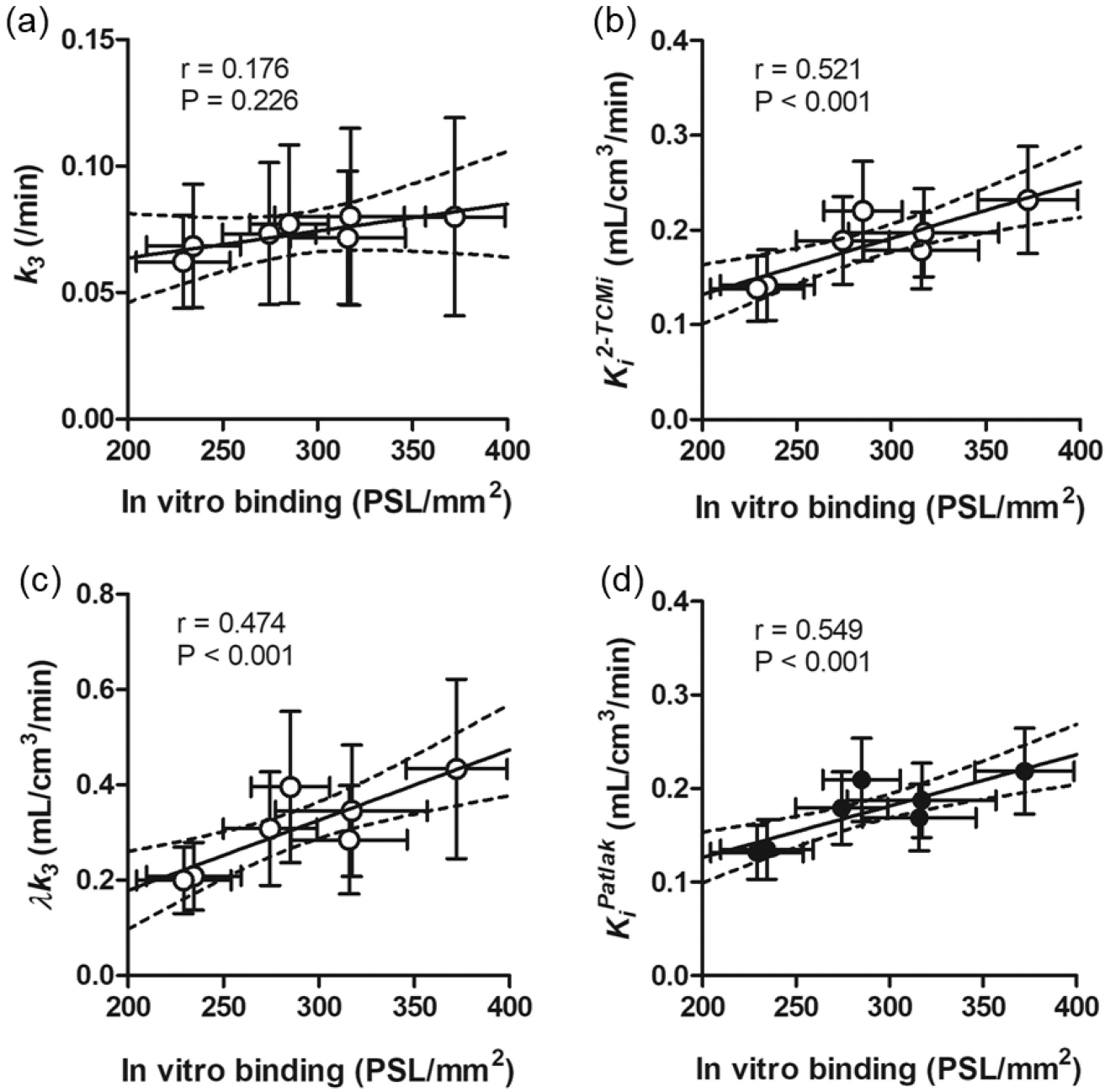

Figure 5.

Correlations between kinetic parameters from the PET studies and in vitro binding on autoradiograms. (a): k_3 vs. in vitro binding; (b): $K_i^{2\text{-}TCMi}$ vs. in vitro binding; (c): λk_3 vs. in vitro binding; (d): K_i^{Patlak} vs. in vitro binding. The regression lines in each graph show the 95% confidence intervals (dotted lines). Respective correlation coefficients (r) and P values are shown adjacent to each scatter plot.

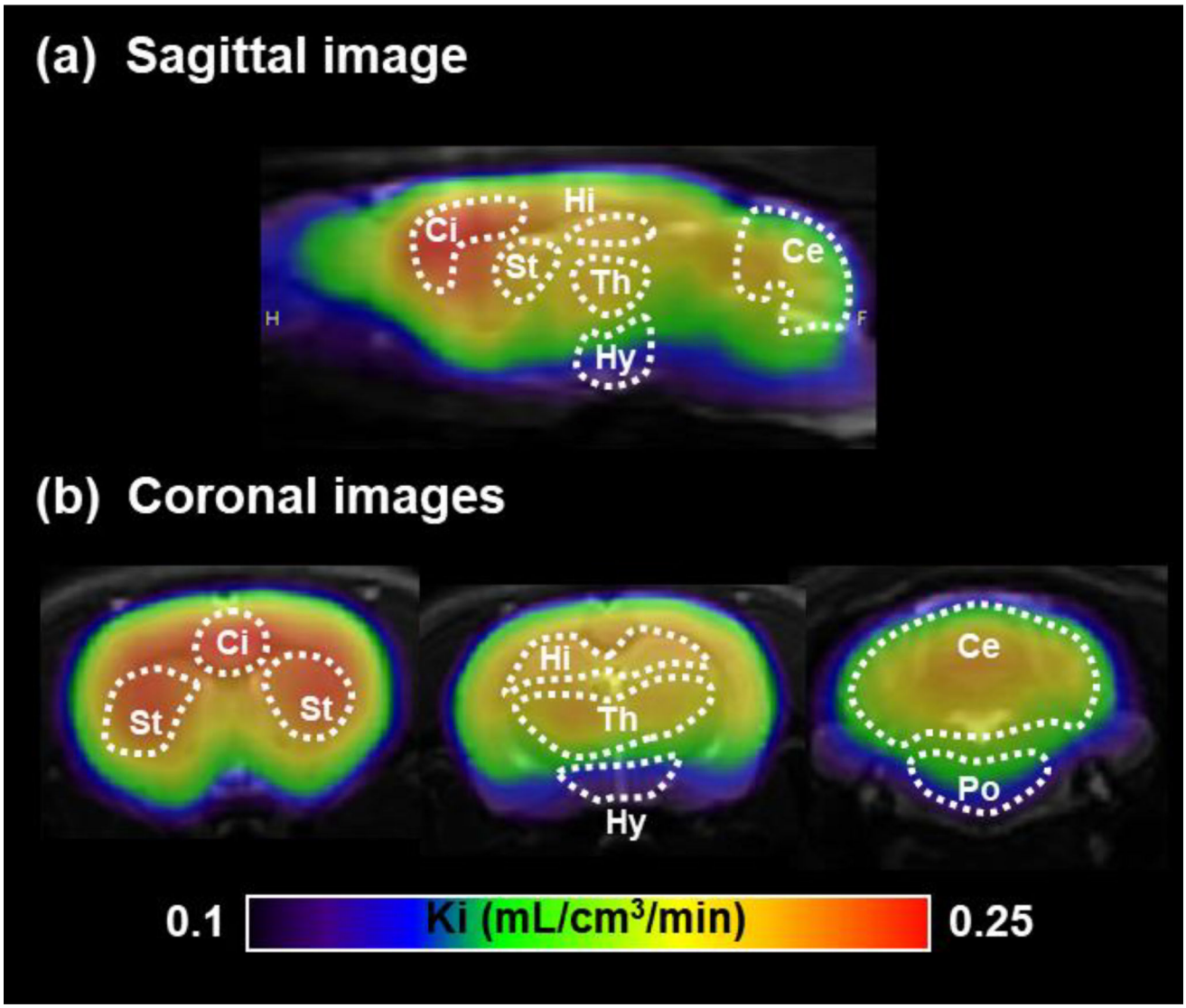

Figure 6.

Averaged (n = 7) parametric PET/MRI images based on K_i value. The sagittal slice (a) was located 1 mm lateral to the bregma and coronal slices (b) were located 0, −3, and −12 mm from the bregma. Ci, cingulate cortex; St, striatum; Hi, hippocampus; Th, thalamus; Hy, hypothalamus; Ce, cerebellum; Po, pons.

Table 1

Full kinetic parameters of PET with [^{11}C]SAR127303.

Region	2-TCMi						Patlak plot	
	K_1 (mL/cm^3/min)	k_2 (/min)	k_3(/min)	K_1/k_2(mL/cm^3)	K_i (mL/cm^3/min)	λk_3 (mL/cm^3/min)	Slope (K_i) (mL/cm^3/min)	Intercept (mL/cm^3)
Cingulate cortex	0.68 ± 0.15	0.12 ± 0.04	0.08 ± 0.04	5.88 ± 2.02	0.26 ± 0.09	0.43 ± 0.19	0.24 ± 0.07	6.27 ± 3.39
	(1.8 ± 0.4)	(7.4 ± 2.3)	(6.7 ± 1.7)	(5.9 ± 2.0)	(8.7 ± 2.1)	(9.0 ± 2.5)	(1.1 ± 0.6)	(17.8 ± 18.4)
Striatum	0.67 ± 0.15	0.13 ± 0.04	0.08 ± 0.03	4.62 ± 1.38	0.24 ± 0.08	0.40 ± 0.16	0.23 ± 0.06	6.53 ± 3.94
	(1.4 ± 0.3)	(5.4 ± 1.7)	(4.9 ± 1.3)	(4.3 ± 1.4)	(6.4 ± 1.7)	(6.5 ± 1.9)	(0.8 ± 0.7)	(9.7 ± 7.5)
Hippocampus	0.62 ± 0.14	0.14 ± 0.04	0.08 ± 0.03	4.40 ± 1.21	0.22 ± 0.07	0.35 ± 0.14	0.20 ± 0.06	5.68 ± 3.86
	(1.5 ± 0.3)	(5.6 ± 1.7)	(5.0 ± 1.3)	(4.4 ± 1.4)	(6.6 ± 1.7)	(6.7 ± 1.9)	(0.8 ± 0.8)	(8.2 ± 6.0)
Thalamus	0.68 ± 0.15	0.16 ± 0.04	0.07 ± 0.03	3.19 ± 0.77	0.21 ± 0.07	0.31 ± 0.12	0.19 ± 0.05	5.92 ± 3.82
	(1.4 ± 0.3)	(4.6 ± 1.3)	(4.2 ± 1.1)	(3.5 ± 1.1)	(5.6 ± 1.4)	(5.5 ± 1.5)	(1.1 ± 1.3)	(8.8 ± 6.9)
Hypothalamus	0.61 ± 0.15	0.20 ± 0.05	0.07 ± 0.02	3.28 ± 0.76	0.15 ± 0.05	0.21 ± 0.07	0.14 ± 0.04	4.28 ± 2.19
	(1.7 ± 0.4)	(5.0 ± 1.4)	(4.7 ± 1.1)	(3.7 ± 1.0)	(6.4 ± 1.4)	(6.0 ± 1.4)	(1.3 ± 1.0)	(14.5 ± 12.3)
Pons	0.66 ± 0.17	0.20 ± 0.05	0.06 ± 0.02	4.43 ± 1.16	0.15 ± 0.05	0.20 ± 0.07	0.14 ± 0.04	4.35 ± 2.33
	(1.2 ± 0.2)	(3.5 ± 0.9)	(3.4 ± 0.8)	(2.5 ± 0.7)	(4.5 ± 1.1)	(4.2 ± 1.1)	(0.8 ± 0.5)	(7.9 ± 4.8)
Cerebellum	0.71 ± 0.18	0.18 ± 0.04	0.07 ± 0.03	4.10 ± 1.11	0.20 ± 0.07	0.29 ± 0.11	0.19 ± 0.06	5.39 ± 2.80
	(1.4 ± 0.3)	(4.5 ± 1.2)	(4.1 ± 1.0)	(3.4 ± 1.0)	(5.6 ± 1.3)	(5.3 ± 1.4)	(0.6 ± 0.6)	(7.3 ± 5.7)

Values in parentheses are percentages of coefficient of variation (%COV). Data are represented as mean ± s.d. (n = 7).